Experimental investigation into rock burst proneness of rock materials considering strain rate and size effect

Xiaobin Li[1,2,3], Haoteng Wang[4]*, Ying Zhao[5], Haifang Xue[3] and Lingyun Li[3]

[1]School of Civil Engineering, Chongqing University, Chongqing, China, [2]Qinghai Traffic Construction Management Co., Ltd., Xining, China, [3]Qinghai Xihu Expressway Management Co., Ltd., Xining, China, [4]State Key Laboratory of Eco-hydraulics in Northwest Arid Region, Xi'an University of Technology, Xi'an, China, [5]School of Highway, Chang'an University, Xi'an, China

In deep rock engineering, evaluating the likelihood of rock burst is imperative to ensure safety. This study proposes a new metric, the post-peak dissipated energy index, which accounts for strain rate and size effects in assessment of the rock burst proneness of a rock mass. To investigate rock burst proneness, conventional compression tests were conducted on limestone and slate samples with different length to diameter (L/D) ratios (ranging from 0.3 to 1.5) at four different strain rates (0.005, 0.01, 0.5, and 1.0 s⁻¹). Based on the testing observations, the actual rock burst proneness was classified into three categories (no risk, low risk, and high risk). A new criterion was also established using the post-peak dissipated energy index, which is the ratio of elastic energy to total dissipated energy. The impact of the strain rate and L/D ratio on rock burst proneness was analyzed. The results indicated that increased strain rates cause a strong hardening effect, leading to staged growth of rock burst proneness. However, the rock burst proneness decreases non-linearly with the increasing L/D ratio. The accuracy of the proposed criterion was validated by comparison with existing criteria, demonstrating that the energy-based index ensures a reliable evaluation of the rock burst proneness of a rock mass. The proposed method has excellent potential for practical application in deep rock engineering.

KEYWORDS

rock burst proneness, post-peak dissipated energy index, strain rate, size effect, failure characteristics

1 Introduction

Rock burst is a potential disaster that poses a significant threat to deep rock excavation and mining operations (Cook, 1976; Wang and Park, 2001; Sousa et al., 2017; Keneti and Sainsbury, 2018; Wojtecki et al., 2021; Wang et al., 2022a; Yang et al., 2022a; Wang et al., 2022b; Yang et al., 2022b). This dangerous occurrence is characterized by the high-speed ejection of rock fragments accompanied by loud cracking sounds (Kaiser and Cai, 2012; Li et al., 2021a; Li et al., 2021b; Liu et al., 2022). As ground stress increases and environmental complexity intensifies, the likelihood and impact of rock bursts also rise (Li et al., 2012; Gale, 2018). To ensure mining efficiency and safety, it is necessary to study the prediction of rock burst (Singh, 1989; Cai et al., 2022; Liu et al., 2023). Typically, rock burst proneness is regarded as a prerequisite for determining the likelihood of rock burst (Feng et al., 2015; Liu S

FIGURE 1
Partial group of rock samples.

M et al., 2020). Various criteria have been proposed to assess rock burst proneness, based on factors such as strength, deformation modulus, energy, acoustic emission, and failure characteristics (Kidybiński, 1981; Singh, 1988; Zhang et al., 2009; He et al., 2015; Khosravi and Simon, 2018; Malan and Napier, 2018; Dai et al., 2019; Gong et al., 2019; Yang et al., 2020a; Gong et al., 2020; Liu S M et al., 2020; Gong et al., 2021; Liu et al., 2022). However, the essence of rock burst is the rapid release of stored elastic strain energy (Kidybiński, 1981; Singh, 1988; Konicek and Waclawik, 2018; Dai et al., 2019), making criteria based on energy parameters particularly meaningful for determining rock burst proneness. Examples of such criteria include the stored energy index W_{et} (Kidybiński, 1981) and the modified bursting energy index K_E^P (Liu X L et al., 2020). W_{et} reflects the energy evolution process and is expressed as the ratio of elastic energy to dissipated energy (Kidybiński, 1981). In fact, rock burst phenomena can still occur during the post-peak stage until it enters the residual stage (Gong et al., 2018c). Although K_E^P considers the entire deformation process, this criterion typically underestimates the rock burst proneness of brittle rock (Liu X L et al., 2020; Zhou et al., 2022). To evaluate the risk of rock burst accurately, a new criterion for rock burst proneness is proposed based on the post-peak dissipated energy characteristic of rock deformation.

Considerable progress has been made in investigating the process and mechanism of rock burst from the perspective of stress path and unloading effect (He et al., 2023). However, the size of the rock has a significant impact on rock burst proneness, due to the mechanical properties and spatial structural characteristics of rock (Ai et al., 2016). The laboratory method considers the structural characteristics of a rock mass as the size of the rock sample, and the results of several experiments have shown that the size of the sample negatively affects rock strength due to the end effect (Wang and He, 2023a). However, the size effect of a rock sample on rock burst proneness has received little attention (Wang et al., 2023b). The size effect leads to stress concentration at the rock boundary and subsequently affects the stress adjustment rate of a rock mass (Kahraman, 2002). Thus, the dependence of rock burst proneness on stress adjustment rate is controlled by the size effect (Dai et al., 2022). Furthermore, the combined effect of high ground stress and external force disturbance is closely related to rock burst occurrence (Du et al., 2016). By enhancing the strain hardening effect, increasing the strain rate

leads to a strong brittleness deformation of rock, making it an essential factor in energy release-induced rock burst (Liu et al., 2023).

To effectively predict rock burst, it is crucial to establish a dependable criterion for rock burst proneness. For this study, conventional compression tests were conducted on samples of limestone and slate with various length-to-diameter (L/D) ratios, under four different strain rates, to investigate proneness to rock burst. A revised index, the post-peak dissipated energy index, was introduced to assess the rock burst proneness of a rock mass, taking into account the strain rate and size effects. Correspondingly, a new criterion has been developed, which can be used to calculate the ratio of elastic energy to total dissipated energy. The practical utility and accuracy of the new criterion were validated through testing.

2 Test method

The uniaxial compressive test is widely used to assess rock burst proneness (Singh, 1988). Strain rate and size effect both influence rock burst proneness (Masoumi et al., 2016; Rybacki et al., 2016; Tang et al., 2002; Tarasov and Potvin, 2013; Yumlu and Ozbay, 1995). According to the principle of thermodynamics, it is assumed that there is no heat exchange between the external environment and the sample during the loading process. Thus, input energy is converted into elastic energy and dissipated energy. The conventional compression test was carried out on two rock types to obtain the energy parameters.

2.1 Rock material

Two types of rock, limestone (sedimentary rock) and slate (metamorphic rock), were obtained from a tunnel construction site in Qinling Mountain, Shaanxi Province, China. During the sampling process, a strong rock burst and a series of residual rock bursts were observed in the field with a burial depth of 1 km. Due to the effects of mineral distribution and composition on the mechanical properties of rock, it was necessary to conduct SEM to investigate differences in mineral composition. The SEM results indicated that the majority of mineral particles in the limestone were lime mud (accounting for 68% of mineral content) and volcanic
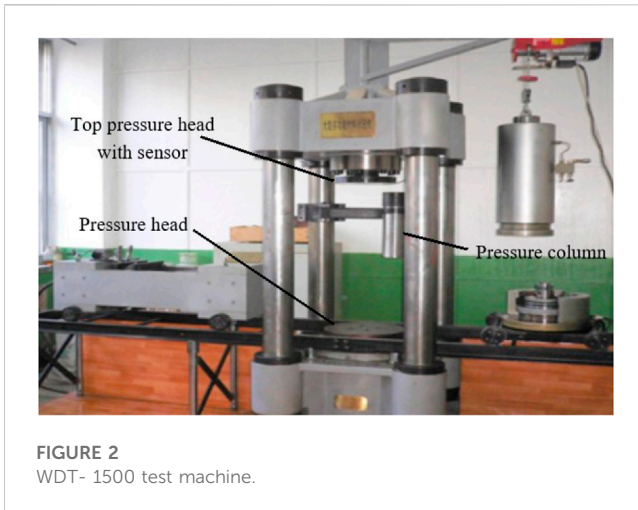
FIGURE 2
WDT- 1500 test machine.

chips (accounting for 24% of mineral content), with accompanying small amounts of pyrite (accounting for 6% of mineral content). These particles were crystallized in a manner that caused a small number of pores in the framework. The slate was composed of flake potash feldspar. In addition, the strong heterogeneity of slate was manifested in the distribution of layered structure. Since the typical layered structure has a strong effect on the mechanical properties of slate, the direction of each sample coring was perpendicular to the slate layer.

According to ISRM recommendations for compression tests (ISRM, 2007), the rock samples were processed into cylindrical shapes with different L/D ratios as follows. The rock specimens had a constant diameter of 50 mm and were of four different lengths (18, 42, 66, and 90 mm for limestone and 18, 24, 48, and 84 mm for slate), as shown in Figure 1.

2.2 Loading method

A series of unconfined compression tests were conducted on the WDT-1500 testing machine (shown in Figure 2). The maximum achieved load of 1800 kN can be applied by the bottom pressure head on the sample. The load and displacement sensors were installed in the top head, which detected a maximum axial displacement of 100 mm and lateral displacement of 5 mm. The error range of axial load and displacement was controlled within 0.1%. Moreover, the loading equipment was installed with three additional systems: a digital control system, a detection system, and a hydraulic loading system. The specific test steps satisfied the recommendations of the ISRM (2007). There was a pressure column upon the sample to concentrate the load on the center axis of the sample. In order to minimize the friction caused by the increased load, a spherical seat was located between the upper surface of the pressure column and the top pressure head. Similarly, two thermally hardened plates were placed on the upper and lower surfaces of the sample to eliminate friction. The conventional compression test was conducted at different loading rates to obtain the uniaxial compressive strength and elastic modulus of the rock. To ensure the consistency of the loading

effect on samples of different sizes (ISRM, 2007), the strain rate ε_e was introduced as

$$\varepsilon_e = \frac{d\varepsilon}{dt} = \frac{(dl/dt)}{l} = \frac{u}{l}, \tag{1}$$

where ε_e represents the strain rate, u is the loading rate, and l is the length of the rock sample.

To study the variation of rock burst proneness according to different strain rates, four strain rates (0.005, 0.01, 0.5, and 1.0 s^{-1}) were considered based on the typical range of strain rate ε_e associated with rock burst (Wasantha et al., 2015). The specific test plan is listed in Table 1. Moreover, to avoid the heterogeneity of the rock material (especially the layered structure of slate), the average mechanical parameter from more than three samples under the same conditions was used in subsequent investigation.

3 Revised criteria for rock burst proneness

Several criteria indicating rock burst proneness (Kidybiński, 1981; Singh, 1988; Zhang et al., 2009; He et al., 2015; Khosravi and Simon, 2018; Malan and Napier, 2018; Yang et al., 2018; Dai et al., 2019; Gong et al., 2019; Gong et al., 2020; Gong et al., 2021; Liu X L et al., 2020) have been reported. Although these criteria analyze the actual conditions of rock burst from different perspectives, the rapid release of stored energy is the essence of rock burst (Cook, 1976; Khosravi and Simon, 2018). During rock burst, the stored elastic energy is consumed by the ejection of rock fragments and dissipated through crack deformation of the rock mass. In particular, the ratio of elastic energy the dissipated energy, namely, W_{et}, is widely used to evaluate rock brittleness (Gong et al., 2019) and rock burst proneness (Kidybiński, 1981). The W_{et} index is determined when rock undergoes yield deformation until failure (the corresponding stress level progresses from 80% to 90%). According to Figure 3, W_{et} can be obtained by

$$U = \int_0^{\varepsilon_1} \sigma d\varepsilon, \tag{2}$$

$$U^e = \frac{\sigma_c^2}{2E}, \tag{3}$$

$$U^d = U - U^e = \int_0^{\varepsilon_1} \sigma d\varepsilon - \frac{\sigma_c^2}{2E}, \tag{4}$$
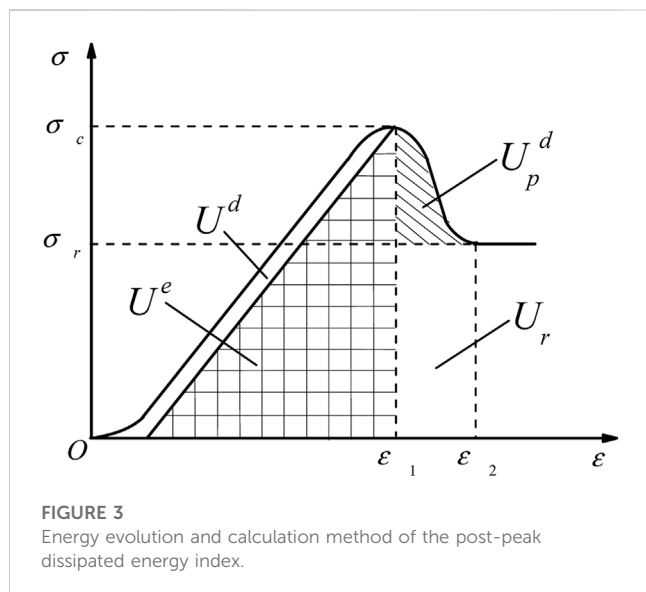
$$W_{et} = \frac{U^e}{U^d}, \tag{5}$$

where σ_c and ε_1 are the UCS and corresponding failure strain, respectively, E is the elastic modulus, and W_{et} is the stored energy index. There are three categories of rock burst proneness quantified by W_{et} (Kidybiński, 1981):

$$\begin{cases} W_{et} \geq 5, & \text{high risk,} \\ 2 \leq W_{et} \leq 4.99, & \text{low risk,} \\ W_{et} < 2, & \text{no risk.} \end{cases} \tag{6}$$

The W_{et} index reveals the essence of rock burst occurrence from a theoretical perspective. Nevertheless, the determination of the W_{et} index is only dependent on the pre-peak energy storage characteristic corresponding to the most violent rock burst. During the excavation process, rock failure induced by stress

TABLE 1 Test method and sample serial number.

Rock type	No.	L/D ratio	Strain rate ε_e (s⁻¹)	Rock type	No.	L/D ratio	Strain rate ε_e (s⁻¹)
Limestone	L-1-1	0.3	0.005	Slate	S-1-1	0.3	0.005
	L-1-2		0.01		S-1-2		0.01
	L-1-3		0.5		S-1-3		0.5
	L-1-4		1		S-1-4		1
	L-2-1	0.4	0.005		S-2-1	0.7	0.005
	L-2-2		0.01		S-2-2		0.01
	L-2-3		0.5		S-2-3		0.5
	L-2-4		1		S-2-4		1
	L-3-1	0.8	0.005		S-3-1	1.1	0.005
	L-3-2		0.01		S-3-2		0.01
	L-3-3		0.5		S-3-3		0.5
	L-3-4		1		S-3-4		1
	L-4-1	1.4	0.005		S-4-1	1.5	0.005
	L-4-2		0.01		S-4-2		0.01
	L-4-3		0.5		S-4-3		0.5
	L-4-4		1		S-4-4		1

FIGURE 3
Energy evolution and calculation method of the post-peak dissipated energy index.

considered the post-peak dissipated energy U_p^d and used to improve the criteria for rock burst proneness. According to Figure 3, the post-peak dissipated energy U_p^d, consumed from the post-peak stage to residual stage, can be calculated as

$$U_p = \int_{\varepsilon_1}^{\varepsilon_2} \sigma d\varepsilon, \qquad (7)$$

$$U_p^d = U_p - U_r = \int_{\varepsilon_1}^{\varepsilon_2} \sigma d\varepsilon - \sigma_r(\varepsilon_2 - \varepsilon_1), \qquad (8)$$
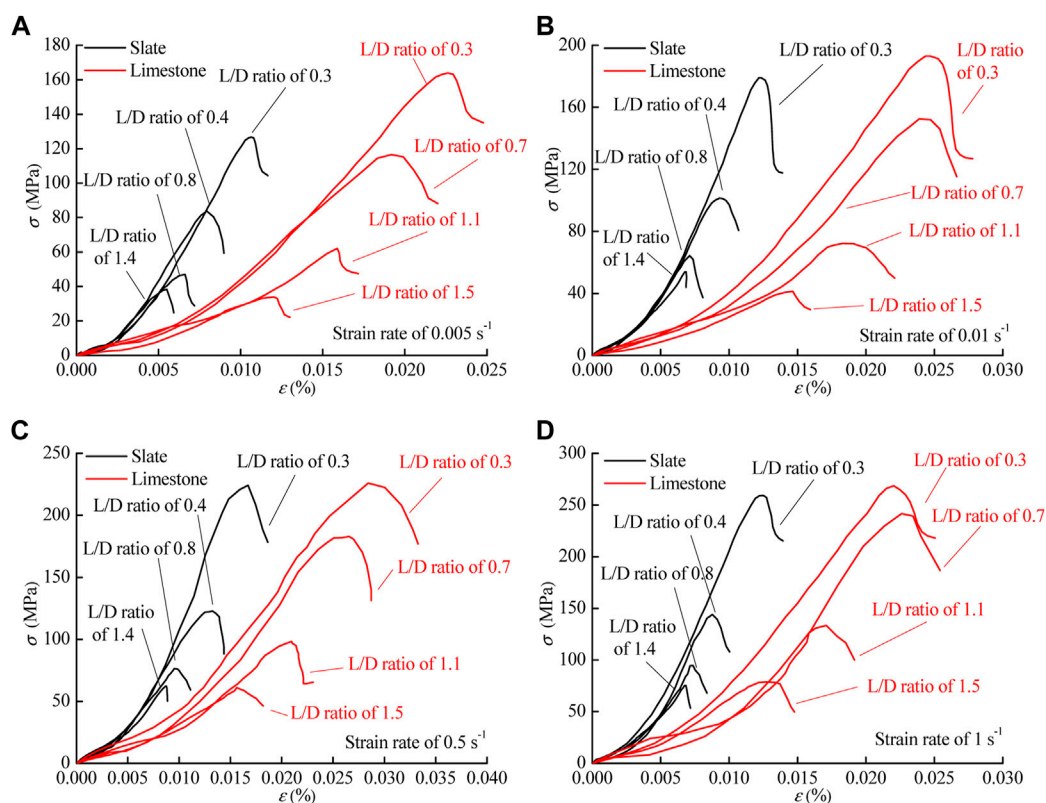
where σ_r is the residual strength and ε_2 is the strain when first entering the residual stage. The post-peak dissipated energy index W_{et}^p is calculated as

$$W_{et}^p = \frac{U^e}{U^d + U_p^d}. \qquad (9)$$

4 Analysis and results

4.1 Mechanical properties and energy storage characteristics

To obtain the energy characteristics during rock deformation to failure, the stress–strain curve under different strain rates and L/D ratios is shown in Figure 4. Several deformation stages can be identified in the stress–strain curve: the compaction stage, elastic stage, yield stage, and residual stage. For limestone, the curve of the initial compaction stage is longer than that for slate. This indicates that the mineral composition and structure of limestone are relatively loose. Limestone specimens have been shown to

disturbance is manifested in two modes, spalling and rock burst (Diederichs et al., 2004). Spalling (the progressive failure of a rock mass) is identified as a precursor to rock burst (Martin and Maybee, 2000; Diederichs, 2007). As ground stress increases, spalling evolves into rock burst (Mazaira and Konicek, 2015). Owing to the instability of the stress adjustment during the excavation process, it is believed that spalling and rock burst occur at the same time until the stress state is stabilized (Gong et al., 2018a; b). This judgment of rock burst should involve the rock deformation before entering the residual stage. The dissipated energy consumed after peak is

FIGURE 4
Stress–strain curve of slate and limestone under different loading rates. **(A)** 0.005s⁻¹, **(B)** 0.01s⁻¹, **(C)** 0.5s⁻¹, and **(D)** 1s⁻¹.

undergo greater deformation until they are at maximum density (Konsztowicz, 2010). The elastic modulus of rock was calculated as the slope of the second stage of the curve in investigation of the influence of scale effect and strain rate. An obvious yield stage was observed in the stress–strain curve of limestone. This phenomenon indicated a strong plastic deformation in this stage. Due to strong brittleness, slate demonstrated a rapid stress drop after the elastic deformation stage. The energy parameters U, U^e, U^d, and U_p^d are calculated in Eqs. (2), (3), (4) and (8), as shown in Table 2. The expression of these energy parameters is in the form of energy density (kJ/m³) to eliminate the effect of rock column volume differences.

The relationship between the UCS and L/D ratio is shown in Figure 5. As the L/D ratio increased, the UCS showed a non-linear decreasing trend. The L/D ratio-dependent variation of UCS gradually stabilized when the L/D ratio reached 1.5. The elastic modulus presented a decreasing trend with increasing L/D, similar to that of UCS, as shown in Figure 6. This indicates that the L/D ratio has a negative effect on the mechanical performance of limestone and slate. It is worth noting that the elastic modulus of limestone decreased linearly. To explain this result, the typical failure characteristics of samples with different L/D ratios are presented in Table 3. For slate and limestone, the failure characteristic changed from complex to single with the increasing L/D ratio. Due to the relatively short stress path of the specimen with a low L/D ratio, the stress concentration phenomenon at the end of the specimen generated a large amount of friction between the pressure head

and the end face of the sample (Tekalur and Sen, 2011). This end friction effect reflects a heterogeneous stress distribution at the end face. In order to maintain the integrity of the rock under mechanical compression, the stress distribution is frequently adjusted. Therefore, there are various failure characteristics observed in rock samples (Walton et al., 2019). When the L/D ratio reaches 1.5, limestone and slate undergo split failure and shear failure, respectively. The typical failure characteristic can be explained in terms of mineral composition and structure. For slate, its typical clastic structure contains a lot of pores at the clastic junction. When the sample enters the critical state of elastoplastic deformation, the stress path passes the weak area of the clastic structure and forms a plastic deformation zone (Quiñones et al., 2017). As the axial load increased constantly to exceed the yield limit of the rock, the stress path penetrated the specimen to form a shear sliding surface. The microstructural properties of the limestone skeleton suggested a muddy supporting texture. When a compressive load was applied, cracks expanded along the cemented boundary of lime mud particles. Therefore, the limestone exhibited splitting failure under compressive load.

The energy indices U, U^e, U^d, and U_p^d of limestone and slate were calculated using Eqs 2–4 to obtain the data distribution of energy storage, as shown in Table 3 and Figure 7. As the input energy U increased, both the elastic energy U^e and dissipated energy U^d showed a linear growth trend. This typical trend is based on the linear energy storage law (Gong et al., 2020). There is an intercept in the fitting formula with a value of approximately 5% of U^e. The

TABLE 2 Mechanical properties and two indices, W_{et} and W_{et}^p, of rock burst proneness for limestone and slate.

Rock type	L/D ratio	ε_e	E	UCS	U^e	U^d	$U_{post-peak}$	W_{et}	U^p	W_{et}^p
		(s⁻¹)	(GPa)	(MPa)	(kJ/m³)	(kJ/m³)	(kJ/m³)		(kJ/m³)	
Slate	0.3	0.005	8.70	126	687	266	389	2.58	25.5	2.36
		0.01	9.75	179	883	212	308	4.17	25.7	3.71
		0.5	17.8	233	1261	165	233	7.64	26.5	6.59
		1.0	21.5	259	1803	195	283	9.25	39.4	7.69
	0.4	0.005	8.08	82.8	353	137	196	2.58	56.5	1.82
		0.01	9.18	101	442	142	203	3.11	46.1	2.35
		0.5	14.3	122	838	158	227	5.30	32.9	4.39
		1.0	18.6	144	1092	169	243	6.46	24.5	5.64
	0.8	0.005	7.77	47.7	138	86.7	120	1.59	8.55	1.45
		0.01	8.45	63.7	251	105.9	148	2.37	26.2	1.90
		0.5	13.1	76.3	345	89.9	124	3.84	47.5	2.51
		1.0	15.5	95.2	439	94.2	131.3	4.66	39.8	3.28
	1.4	0.005	7.56	39.6	95.4	53.5	70.3	1.78	9.80	1.51
		0.01	8.25	54.0	111.6	65.6	88.4	1.70	10.3	1.47
		0.5	10.2	62.1	135.3	62.8	84.2	2.15	10.3	1.85
		1.0	12.4	75.5	172	56.7	75.1	3.03	13.4	2.45
Limestone	0.3	0.005	11.1	164	718	212	308	3.39	12.9	3.19
		0.01	19.5	193	1103	223	324	4.95	11.1	4.71
		0.5	21.2	226	1523	232	338	6.56	23.0	5.97
		1.0	29.2	268	1978	261	381	7.58	26.7	6.88
	0.7	0.005	8.39	116	530	229	333	2.31	9.11	2.23
		0.01	13.3	152	649	189	273	3.43	10.1	3.26
		0.5	16.8	183	685	173	249	3.96	8.95	3.76
		1.0	24.5	241	841	135	192	6.23	7.09	5.92
	1.1	0.005	4.4	62.1	301	151	216	1.99	11.8	1.85
		0.01	7.58	72.3	355	144	206	2.47	9.14	2.32
		0.5	13.0	98.2	400	138	197	2.90	13.7	2.64
		1.0	18.0	133	475	102	143	4.66	12.7	4.14
	1.5	0.005	3.90	34.3	153	97	135	1.58	10.8	1.42
		0.01	6.11	41.6	196	112	158	1.75	8.00	1.63
		0.5	13.5	61.7	227	112	158	2.03	6.07	1.92
		1.0	15.1	79.5	305	100	140	3.05	3.33	2.95

fitting coefficient R^2 ranged from 0.94 to 0.99, indicating an accurate linear correlation between the energy storage and dissipation. For slate and limestone, the slope value of U^e versus U represents the storage ability of elastic energy. The figure demonstrates that the energy storage ability of slate was stronger than that of limestone (slope values were 0.93 and 0.71 for slate and limestone, respectively). The difference in slope value is related to the

deformation characteristics of slate. The stress–strain curves in Figure 4 indicate that slate samples usually underwent brittle failure, which hardly contained a yield stage. The typical failure characteristic indicated that the input energy transformed into elastic energy stored in the sample, instead of being dissipated by crack propagation (Wang et al., 2021). Moreover, a linear correlation between the post-peak dissipated energy U_p^d and pre-
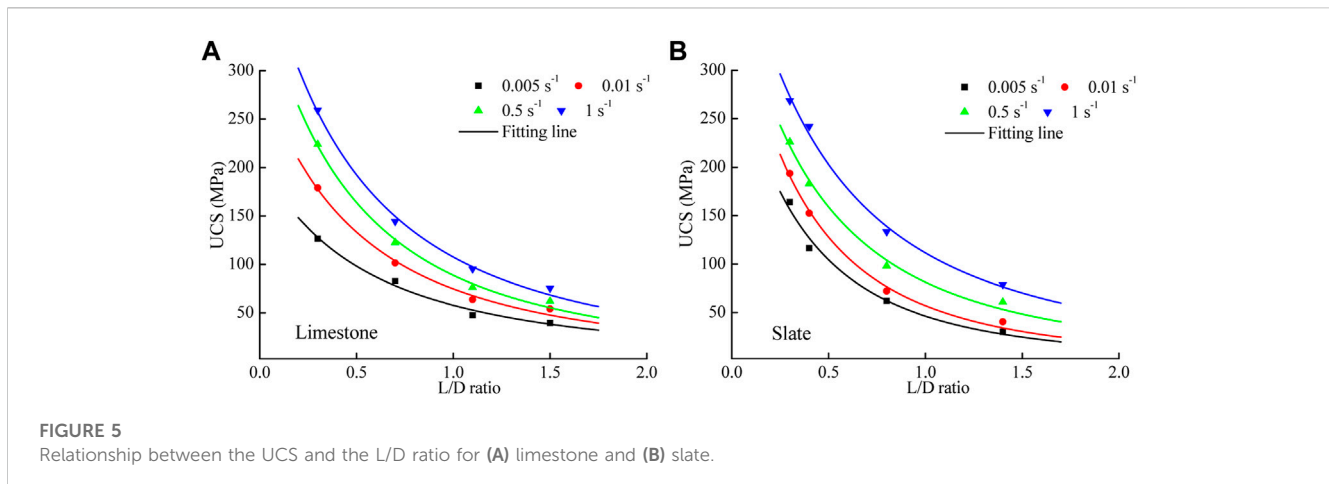
FIGURE 5
Relationship between the UCS and the L/D ratio for **(A)** limestone and **(B)** slate.

peak dissipated energy U^d is presented in Figure 7B. The linear correlation between U_p^d and U^d can be explained by the failure process. The failure process of limestone and slate followed a similar principle in that the failure path extended along the weakest part. As for the post-peak stage, energy was dissipated through the friction of the pre-existing crack surfaces when the applied loading on the sample was increased.

To obtain the effects of L/D and strain rate on these linear energy characteristics, the correlation between the ratio of elastic energy to input energy and two influence factors are presented in Figure 8. Due to the large range of strain rates, the variation of strain rate is usually described as a semi-log equation. The error bar represents the range of the U^e/U values under the same condition to emphasize the influence of individual factors. The effects of L/D and strain rate on the linear energy characteristics were observed in limestone and slate. As the strain rate ε_e increased, U^e/U increased in segments. When ε_e had a range from 0.01 to 0.5 s^{-1}, the increased value of U^e/U averaged 8% for slate and limestone. The elastic deformation capacity of rock can be characterized by U^e/U. With increasing ε_e, the strain rate-hardening effect becomes more significant, resulting in a reinforcement of elastic deformation under compressive load. The size effect of rock on the linear energy characteristic is demonstrated as a linear trend. The difference in slope values between slate and limestone (33.3%) revealed the effect of slate brittleness on the failure characteristics induced by the size of the sample. There was an apparent stress concentration at end face caused by size effect. Stress concentrations not only created cracks but also caused friction to dissipate energy. The detrital distribution of slate was beneficial for crack propagation and energy dissipation. Therefore, the decreased U^e/U of slate was more obvious than that of limestone.

4.2 Proposed criteria for rock burst proneness

Failure of rock specimens is accompanied by the rapid propagation of cracks and ejection of rock chips (Małkowski and Niedbalski, 2020). The failure characteristics are affected by the energy storage property of a rock mass. Pre-stored energy releases rapidly and transforms into the kinetic energy consumed by the ejection of rock chips (Feng et al., 2021). The rapid energy conversion is similar to the mechanism of rock burst in a mine (Cai et al., 2021). Nevertheless, it is difficult to capture rock fragments and calculate the total kinetic energy to determine rock burst proneness (Gong et al., 2021). In the actual rock burst, failure sound, observed size distribution of rock fragments, and failure characteristics are considered the standard. To establish criteria for rock burst proneness based on the W_{et}^p index, the actual failure situation of slate and limestone was recorded. Table 4 shows the typical failure modes of limestone and slate under the maximum and minimum strain rates. According to the failure characteristics under different conditions, the rock burst proneness was characterized into three categories (high risk, low risk, and no risk). The specific descriptions of the three categories for actual rock burst proneness are included as follows.
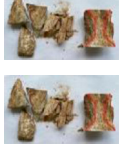
No risk of rock burst: At a low strain rate, the slate specimens with an L/D ratio of 1.5 and 1.8 had only one oblique shear crack, accompanied by a few scattered slate particles, as shown in Table 4. There was no obvious sound upon specimen failure. Moreover, the rock fragments slid down along the failure surface under the action of gravitational potential energy instead of being ejected.

Low risk of rock burst: For most slate and limestone specimens, large fragments could be observed to fall off, but the specimens retained their main shape. The limestone with low-risk rock burst proneness showed typical split failure. Only a small amount of rock particles had been observed to eject at low velocity. Taking the limestone specimen with an L/D ratio of 1.1 at low strain rate, a majority of limestone flakes were distributed on the pressure head, and only a few small pieces were ejected on the pressure platform.

High risk of rock burst: The failure modes of slate specimens and limestone specimens with the L/D ratio of 1.1 under high strain rate presented typical failure characteristics of rock burst. The specimens were broken into many rock chunks and particles that were no more than 3.0 cm in size, which were ejected on the platform at high velocity. Therefore, the failure characteristics of high risk of rock burst can be described as a large amount of rock debris and particles ejected at a high speed, accompanied by a

TABLE 3 Failure characteristics of slate and limestone with different L/D ratios under different strain rates.

Rock type	L/D ratio	Failure characteristics		
		Strain rate of 0.005 s^{-1}	Strain rate of 1.0 s^{-1}	Description
Slate	0.3			X-shape shear failure
	0.4			X-shape shear failure
	0.8			Oblique shear failure
	1.4			Oblique shear failure
Limestone	0.3			Oblique shear failure and split failure
	0.7			Split failure and X-shape shear failure
	1.1			Split failure and shear failure
	1.5			Split failure at a low rate and X-shape shear failure at a high rate

strong crackling sound and fall on the platform when the specimen disintegrated.

According to the actual rock burst proneness determined by the failure characteristics, the post-peak dissipated energy index W_{et}^{p} of limestone and slate were classified into three categories, no risk, low risk, and high risk, as shown in Figure 9A. The risk level of rock burst proneness improved with increasing W_{et}^{p} values. The W_{et}^{p} data points indicate a quantitative correlation between the W_{et}^{p} value and the actual rock burst proneness. In summary, the W_{et}^{p} index is a feasible method for evaluation of rock burst

proneness, and the specific criterion for rock burst proneness is confirmed as

$$\begin{cases} W_{et}^{p} > 5.5, & \text{high risk,} \\ 2.5 \leq W_{et}^{p} \leq 5.5, & \text{low risk,} \\ W_{et}^{p} < 2.5, & \text{no risk.} \end{cases} \tag{10}$$

The occurrence of rock burst is closely associated with stored energy release. By considering post-peak energy dissipation, the rock burst proneness can be modified to adapt to the actual situation. Compared with the criterion for rock burst proneness using W_{et}, the
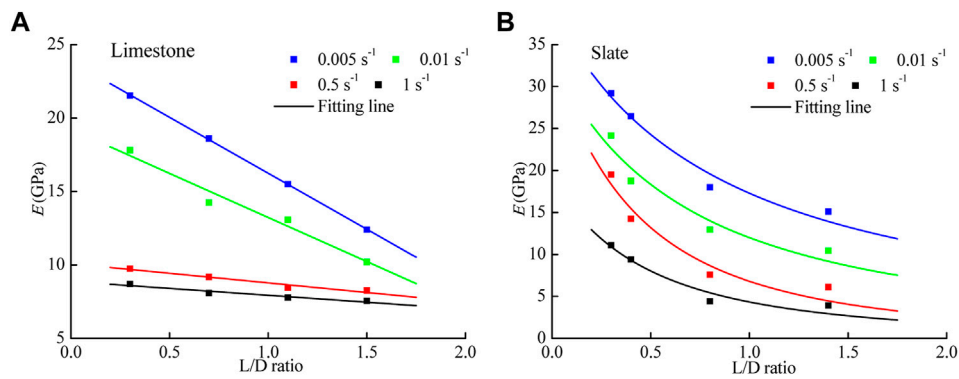
FIGURE 6
Relationship between the elastic modulus and the L/D ratio under different strain rates. **(A)** Limestone and **(B)** Slate.
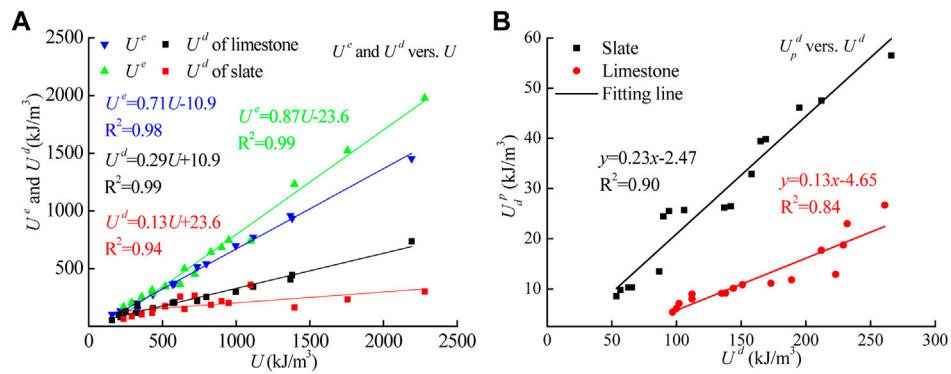
FIGURE 7
Relationship between **(A)** U^e and U^d versus U and **(B)** U_p^d versus U^d for limestone and slate.
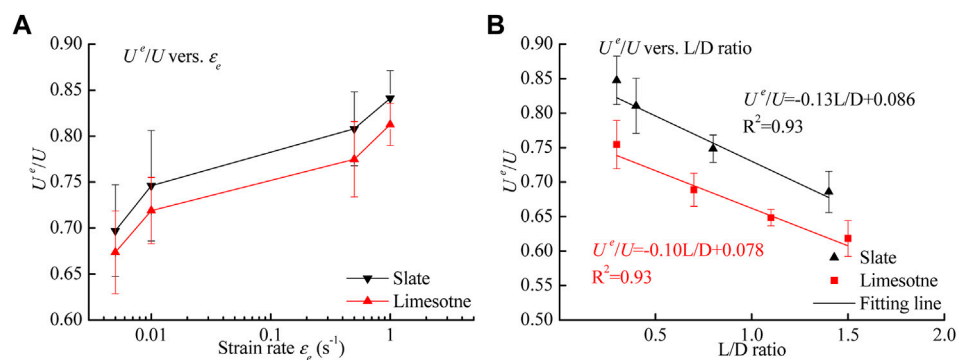
FIGURE 8
Effect of the strain rate and L/D ratio on the linear energy characteristics. **(A)** strain rate and **(B)** L/D ratio.

three criterion categories of the revised rock burst proneness, determined using the W_{et}^p index, increased by 0.5. Comparison between the actual rock proneness and the rock burst criterion (Eq. 6) proposed by Kidybiński (1981) is shown in Figure 9B. Obviously, the data point distribution of W_{et} is more dispersed than that of W_{et}^p.

Taking slate as an example, when L/D ratio is 0.8 and strain rate is 0.5 s^{-1}, the W_{et} value is calculated as 5.30 and identified as at high risk of rock burst. The revised index W_{et}^p calculated under the same conditions identified the sample as low risk, with a value of 4.39. The failure characteristic presented only a small amount of debris falling

TABLE 4 Fitting formula of W_{et}^p versus L/D ratio.

Rock type	ε_e (s⁻¹)	Fitting function	Rock type	ε_e (s⁻¹)	Fitting function
Limestone	0.005	$W_{et}^P=4.26\ (1+L/D)^{-1.2}$, $R^2=0.98$	Slate	0.005	$W_{et}^P=2.97\ (1+L/D)^{-1.2}$, $R^2=0.86$
	0.01	$W_{et}^P=7.24\ (1+L/D)^{-1.6}$, $R^2=0.99$		0.01	$W_{et}^P=4.89\ (1+L/D)^{-1.5}$, $R^2=0.85$
	0.5	$W_{et}^P=9.39\ (1+L/D)^{-2.2}$, $R^2=0.99$		0.5	$W_{et}^P=11.6\ (1+L/D)^{-2.2}$, $R^2=0.90$
	1.0	$W_{et}^P=9.67\ (1+L/D)^{-1.7}$, $R^2=0.88$		1.0	$W_{et}^P=12.7\ (1+L/D)^{-2.5}$, $R^2=0.92$

TABLE 5 Summary of rock burst proneness based on three indices from Liu S M et al. (2020), Małkowski and Niedbalski (2020), and Bukowska (2005).

Rock type	L/D	ε_e (s⁻¹)	M (GPa)	W_{TG}	P_{ES} (kJ)	K_E^P	Rock type	L/D	ε_e (s⁻¹)	M (GPa)	W_{TG}	P_{ES} (kJ)	K_E^P
Slate	0.3	0.005	13.8	0.63	36.9	1.77	Limestone	0.3	0.005	26.5	0.42	46.1	2.33
		0.01	21.0	0.47	90.0	2.87			0.01	17.0	1.15	87.9	3.40
		0.5	16.3	1.10	278	5.41			0.5	8.50	2.49	131	4.51
		1.0	13.5	1.59	385	6.37			1.0	12.8	2.28	324	5.19
	0.4	0.005	12.2	0.66	18.4	1.80		0.7	0.005	17.1	0.49	27.5	1.59
		0.01	20.9	0.44	35.7	2.18			0.01	26.8	0.50	68.8	2.38
		0.5	22.1	0.65	81.1	3.69			0.5	23.7	0.71	126	2.75
		1.0	18.4	1.01	12.8	4.49			1.0	24.1	1.02	346	4.38
	0.8	0.005	25.7	0.30	7.34	1.15		1.1	0.005	21.1	0.21	10.7	1.39
		0.01	22.0	0.38	15.5	1.70			0.01	22.0	0.34	20.1	1.72
		0.5	16.9	0.78	34.5	2.78			0.5	11.3	1.16	63.6	2.03
		1.0	13.4	1.16	58.3	3.34			1.0	13.6	1.33	201	3.32
	1.4	0.005	36.9	0.20	6.32	1.36		1.5	0.005	34.1	0.11	3.90	1.13
		0.01	21.8	0.38	14.3	1.26			0.01	24.5	0.25	6.41	1.24
		0.5	36.8	0.28	23.4	1.61			0.5	21.2	0.64	31.2	1.44
		1.0	28.3	0.44	37.7	2.29			1.0	39.6	0.38	81.0	2.18

FIGURE 9
(A) Relationship between W_{et}^p and actual rock burst proneness and **(B)** comparison between W_{et} and actual rock burst. Note that the sequence of symbols of slate and limestone corresponds to the increasing L/D ratio.
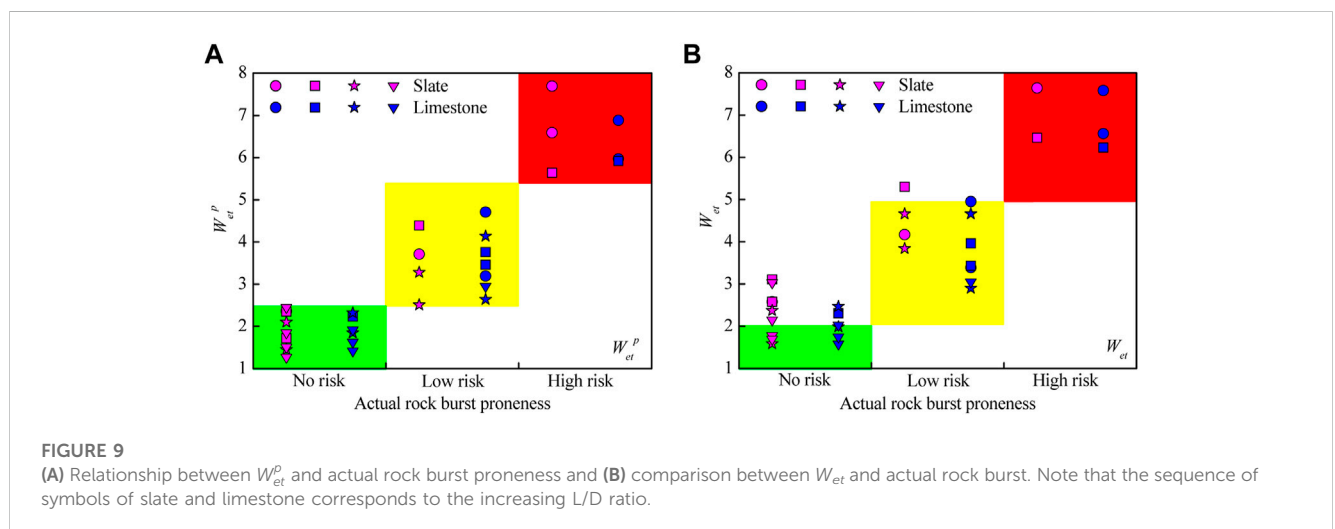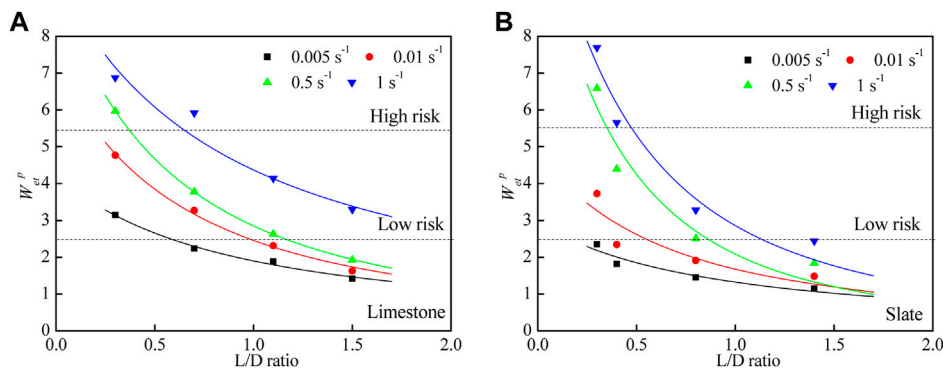
FIGURE 10
Correlation between W_{et}^p and the L/D ratio for **(A)** Limestone and **(B)** Slate.
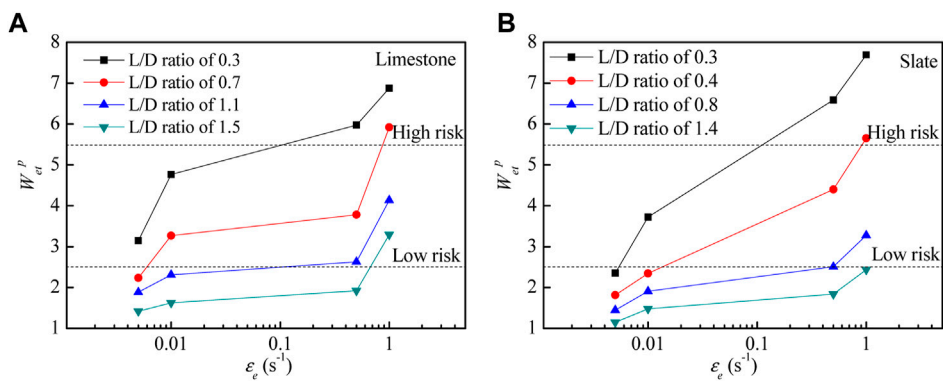
FIGURE 11
Correlation between W_{et}^p and ε_e under various L/D ratio conditions using the semi-log equation for **(A)** Limestone and **(B)** Slate.

on the pressure head, accompanied by a small sound, which suggests that the revised index W_{et}^p provides a more accurate judgment of rock burst proneness.

4.3 Effect of the L/D ratio and strain rate on rock burst

Based on the relationship between the post-peak energy dissipation and failure characteristics, the criterion for rock burst proneness has three categories: no risk, low risk, and high risk. The W_{et}^p value corresponding to the same category of rock burst proneness had a significantly different distribution. This suggests a strong quantitative correlation between W_{et}^p index and rock burst proneness. Thus, the effect of L/D ratio and strain rate on the W_{et}^p index was investigated to clarify the correlation between the post-peak dissipated energy index and actual rock burst proneness, as shown in Figures 10, 11. The influence of L/D ratio on the W_{et}^p index was fitted as a function, as evident in Table 4 and shown in Figure 10. In addition, the dashed line was added in the figure to emphasize the risk categories of actual rock burst. The fitting coefficient R^2 exceeded 0.85, but the R^2 value of slate was relatively smaller than that of limestone. According to Table 3, the rock failure characteristic becomes more typical with the increasing L/D

ratio. This indicates that crack propagation is concentrated around the failure path. The concentration of crack behavior enhances the interaction among cracks (Konsztowicz, 2010). Thus, crack deformation behavior became more frequent to dissipate energy, resulting in a decline of W_{et}^p. Moreover, the reduction of W_{et}^p was affected by strain rate. Especially for slate, the function parameters of strain rate at 0.5 and 1.0 s^{-1} were 200% of that of strain rate at 0.05 and 0.1 s^{-1}. There was a phenomenon of strain hardness in the stage of yield deformation. The acceleration of the strain rate enhanced the strain hardening effect, which extended the yield deformation stage (Lundborg, 1967). As the stored energy increased, the risk of rock burst increased correspondingly. Moreover, the fitting trend was similar to that of UCS, suggesting that the occurrence of rock burst was related to the compressive performance of rock.

For most conditions of limestone and slate, the increase in W_{et}^p with increasing ε_e can be characterized as having three stages, as shown in Figure 11. There was a steady platform stage for W_{et}^p, with an increase of no more than 20% within a strain rate range from 0.01 to 0.5 s^{-1}. As the L/D ratio increased, the plateau stage became more obvious. This suggests that the rate-dependent growth in W_{et}^p has a critical value with variation of L/D ratio. For slate samples with L/D ratios of 0.3 and 0.4, W_{et}^p had a nearly linear increasing trend, and the most violent rock bursts were also observed in these samples. Evolution of energy

FIGURE 12
Variation of W_{et}^{p} with different L/D ratios and strain rates for **(A)** Limestone and **(B)** Slate.
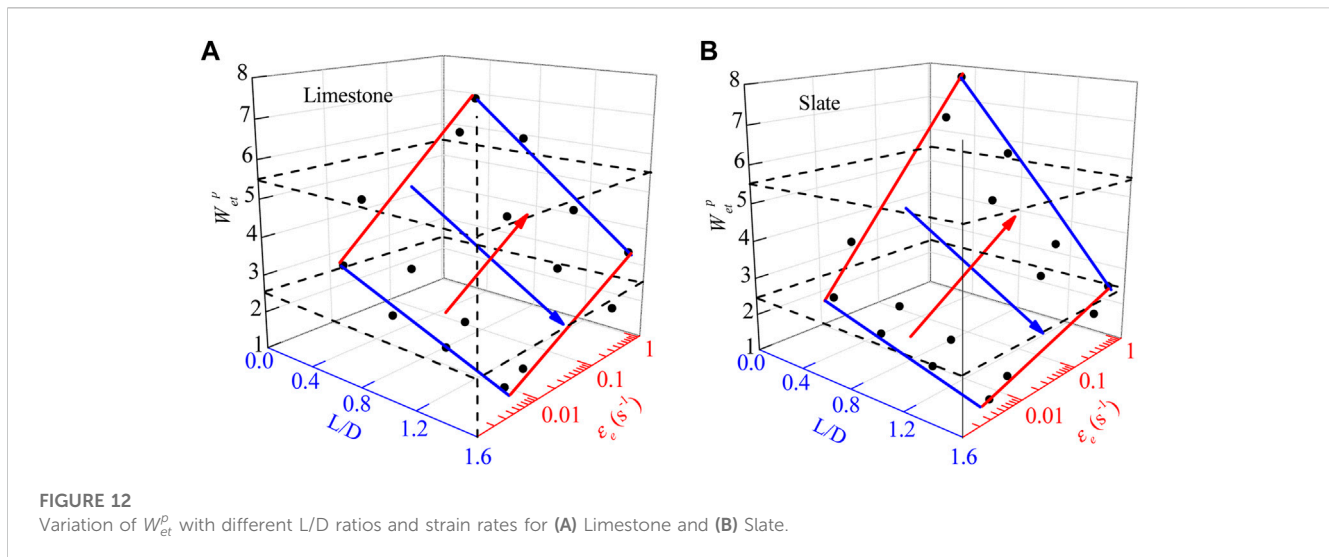
dissipation and release was closely related to the process of rock deformation until failure (Wang et al., 2019). The variation of the failure characteristics was dependent on the inertial effect of rock material under the condition of high-rate compression load. It has been shown that, when the strain rate reaches 0.5 s^{-1} (Luo et al., 2014), the period from crack initiation to rupture of a rock sample becomes shorter (Li et al., 2014). Similar results were obtained from the difference of failure characteristics, as listed in Table 3.

Comparing the curves in Figures 10, 11, it can be observed that the effects of strain rate and scale effect on W_{et}^{p} are opposite. There is a non-linear relationship between the L/D ratio and W_{et}^{p} index. This correlation is similar to the effect of L/D ratio on the UCS. This different trend induced different failure characteristics. Following the least energy consumption law, the failure of rock tends to be typical with variation of L/D ratio. However, the strain hardening effect (Wei et al., 2021) was enhanced by the increasing strain rate and generated the platform stage for the rate-dependent variation of W_{et}^{p}. Taking into account variation of W_{et}^{p} based on the combined effects of scale effect and strain rate, W_{et}^{p} can be obtained as follows:

$$W_{et}^{p} = c + a \cdot \varepsilon_e - b \cdot (L/D), \tag{11}$$

where a, b, and c are the fitting parameters with values of 3.05, 3.67, and 2.62 for limestone and 3.12, 4.27, and 2.21 for slate, respectively. The fitting result is shown in Figure 12, which is marked with a dashed line representing the risk grades of rock burst. The fitting coefficients R^2 of the two rocks were 0.91 and 0.93, indicating an accurate determination of W_{et}^{p}. It should be noted that, for the test, the boundary of the fitting equation was set as an L/D ratio in the range of 0.3–1.5 and ε_e in the range of 0.005–1 s^{-1}.

5 Discussion

5.1 Effect of strain rate and L/D ratio on linear energy characteristics

The process of rock failure is closely related to energy dissipation and storage during energy evolution. Previous studies have indicated that the characteristics of energy dissipation and storage are essential in determining rock burst proneness (Kidybiński, 1981; Li et al., 2014; Wasantha et al., 2015; Gale, 2018; Liu X L, et al., 2020; Gong et al., 2021). To investigate the critical state of rock burst occurrence, this study proposed the post-peak dissipated energy index W_{et}^{p} to evaluate rock burst proneness and considers the effect of strain rate and size. Linear energy characteristics were obtained, which were influenced by variations in the L/D ratio and strain rate ε_e, as demonstrated by segmented growth of U^e/U for slate and limestone in Figure 8. This finding is similar to that reported by Li et al. (2014), who noted that the strain rate has a threshold value of 1×10^{-2} s^{-1} for the sudden release of elastic energy to induce splitting and even rock burst. The rate-dependent effect on rock energy characteristics was also investigated by Wasantha et al. (2015),from the perspective of mineral grain size distribution. The results revealed that the linear energy characteristic presents an increasing trend, resulting in U^e/U not maintaining a constant increasing trend with strain rate. Furthermore, the effect of strain rate on rock burst can be demonstrated through its stress adjustment response (Li et al., 2012). The size effect on rock burst is different from that of strain rate. Su (2004) analyzed size-dependent rock burst tendency from the perspective of changing brittleness and concluded that, at the same diameter, elastic energy is proportional to the L/D ratio. This result is also evident in Figure 8B. As a result, the weakening process of the sample is intensified, leading to increased brittleness (Darbor et al., 2019). From a failure perspective, stress concentration becomes more obvious at the end face of the sample as the L/D ratio decreases (Lundborg N, 1967), and the energy storage process is accelerated, leading to the ejection of rock fragments at a faster speed. These two results illustrate the significant influence of rock size on the energy storage process (Li et al., 2023). To provide a reliable reference for predicting rock burst, these findings emphasize the importance of considering the strain rate and size effects when evaluating rock burst proneness.

To examine the validity of the linear energy principle, data from various types of rocks and rock-like materials (such as coal and concrete) from other literature sources have been introduced. The materials considered in this analysis include gas coal (Gong et al., 2020), TJH coal (Liu S M et al., 2020), ordinary concrete, EPS
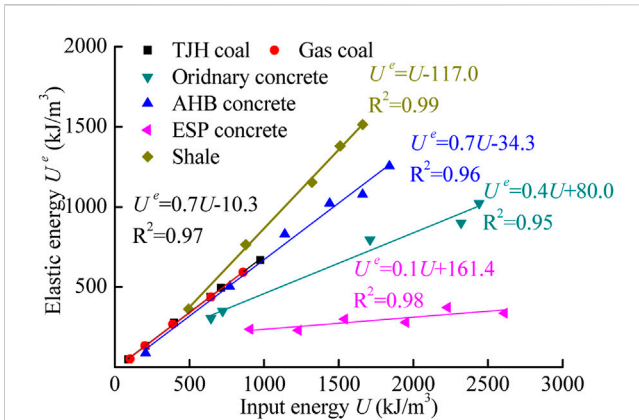
FIGURE 13
Relationship between U^e and U. Sources: shale, Iman et al. (2018); TJH coal, Liu S M et al. (2020); gas coal, Gong et al. (2020); and ordinary, ESP, and AHB concrete, Lu et al. (2017).

concrete, and AHB concrete (Lu et al., 2017), as well as shale (Iman et al., 2018), as shown in Figure 13. The results indicate a strong linear correlation between U^e and U, with a fitting coefficient R^2 over 0.95. The difference in the slope values for different materials reflects their unique energy storage characteristics.

Although gas coal and TJH coal are obtained from different regions (Shaanxi and Shandong provinces, respectively), their energy storage trends are fitted to the same function (marked in black). This suggests that the energy distribution of coal is relatively stable compared to shale and concrete. However, due to the different properties of additive materials in concrete, the energy storage characteristics differ significantly. Under compressive load, the addition of AHB material causes the concrete to undergo crushed failure earlier, thus dissipating a portion of the input energy instead of storing it in the sample. Furthermore, the addition of AHB matrix generates pores at the contact surface, leading to further crack deformation and energy dissipation (Luo et al., 2014). Conversely, the addition of EPS material in concrete plays a key role in buffering the compressive loading to enhance elastic deformation, thereby improving the energy storage ability of the concrete sample (Kirane et al., 2015). The comparative analysis indicates that shale has a stronger ability to store energy than coal or concrete. This is related to the strong brittleness of shale and its elastic energy storage performance.

5.2 Comparative analysis of W_{et}^p on rock burst proneness

Rock burst is characterized by the sudden release of stored elastic strain energy, which results in the high-speed ejection of rock fragments. The intensity of a rock burst depends on the rate of release of elastic energy. After stress adjustment in the rock mass, the stress concentration occurs at the rock mass to generate a rock burst (Feng et al., 2015). To better estimate rock burst proneness, we propose the post-peak dissipated energy index, which is based on the linear energy storage characteristics of rocks. This index accounts for the strain energy dissipation after

failure, resulting in improved accuracy in estimating rock burst proneness.

To assess the effectiveness of the proposed W_{et}^p index in predicting rock burst susceptibility, this study compared it to other indices for analyzing limestone and slate, such as the modified bursting energy index K_E^P (Liu S M et al., 2020), the potential elastic energy index P_{ES} (Małkowski and Niedbalski, 2020), and the rock burst index for rock mass W_{TG} (Bukowska M, 2005). The modified bursting energy index K_E^P, proposed by Liu X L et al. (2020), evaluates the energy release capability of rock by considering its post-failure energy behavior.

$$K_E^P = \frac{U^e}{U_{post-peak}}, \qquad (12)$$

where $K_E^P < 2$ indicates no proneness to rock burst, $K_E^P = 2–5$ indicates low proneness to rock burst, and $K_E^P > 5$ indicates strong proneness to rock burst.

Małkowski and Niedbalski (2020) found that the tendency for rock burst under pressure load can be evaluated by the storage of potential elastic energy. On this basis, the potential elastic energy index P_{ES} was derived using the UCS and elastic modulus as

$$P_{ES} = 500 \frac{\sigma_c^2}{E}, \qquad (13)$$

where P_{ES} (kJ) classifies the rock burst tendency into four grades: $P_{ES} < 40$ indicates no proneness, $40 < P_{ES} < 100$ indicates weak proneness, $100 < P_{ES} < 200$ indicates high proneness, and $P_{ES} > 200$ indicates extreme proneness.

The characteristics of the geo-mechanical system (coal seam-surrounding rock) were analyzed to develop the criterion for rock burst tendency. In accordance with the stress–strain curves of rock mass, post-failure deformation modulus M and Young's modulus E were introduced to assess the rock burst tendency (Bukowska M, 2005):

$$W_{TG} = \frac{M}{E}, \qquad (14)$$

where $W_{TG} < 1$ indicates no proneness to rock burst, $1 < W_{TG} < 2$ indicates little proneness to rock burst, and $W_{TG} > 2$ indicates strong proneness to rock burst.

The modified bursting energy index K_E^P (Liu S M et al., 2020), the potential elastic energy index PES (Małkowski and Niedbalski, 2020), and the rock burst index for rock mass W_{TG} (Bukowska M, 2005) were compared to estimate the burst proneness of limestone and slate, as shown in Figure 14 and Table 5. P_{ES} exhibited a relatively accurate prediction of rock burst compared to K_E^P and W_{TG}. However, one limestone sample with an L/D ratio of 0.7 and a strain rate of 0.5 s^{-1} was overestimated as having high risk of actual rock burst. W_{TG} misjudged numerous cases, particularly those with little and strong risk of rock burst. As rock burst proneness increased, the presented brittleness in rock failure became more apparent. This indicated that an obvious stress drop occurred after the peak, leading to a large value of failure modulus M. However, the brittleness-dependent strain hardening effect led to an enhancement of the elastic deformation capacity of rock, which manifested in an increase in the elastic modulus E. W_{TG} is expressed as the ratio of E to M; therefore, the variation of W_{TG} does not reflect the difference between E and M values in
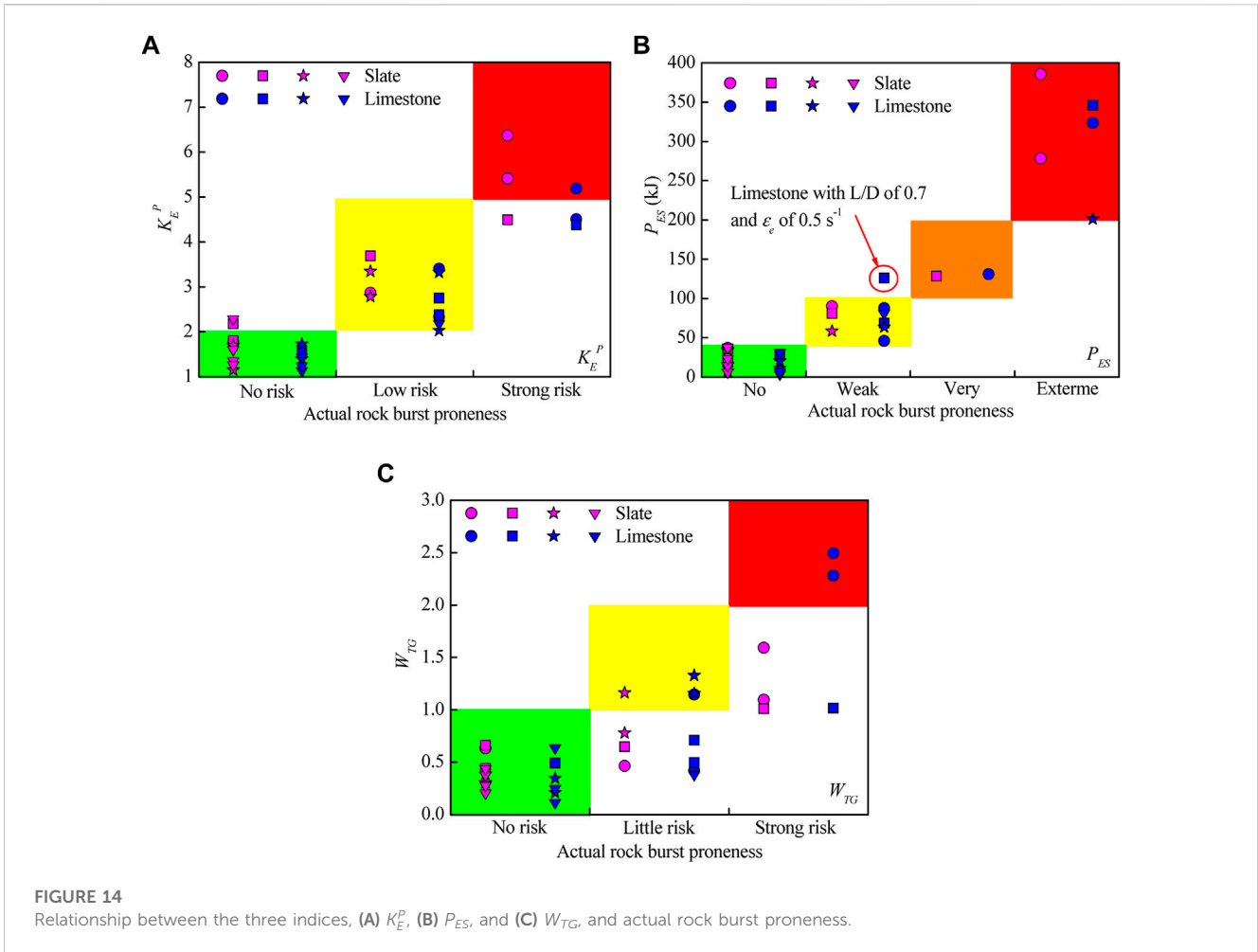
FIGURE 14
Relationship between the three indices, **(A)** K_E^P, **(B)** P_{ES}, and **(C)** W_{TG}, and actual rock burst proneness.

representation of rock burst proneness. Moreover, a small number of K_E^P data points were distributed outside the corresponding category area of rock burst proneness. The K_E^P values of limestone and slate underestimated the low risk of actual rock burst, whereas the proposed index W_{et}^P accurately predicted rock burst proneness. The difference between the U^e and $U_{post-peak}$ used in K_E^P did not reflect the essence of rock burst, which is the release of stored elastic strain energy.

6 Conclusion

Conventional compression tests were carried out on limestone and slate samples under different conditions (including variations in strain rate and sample size). By considering the energy dissipated in the post-peak stage, the W_{et}^P index was proposed to evaluate rock burst proneness. The effects of sample size and strain rate on the W_{et}^P index were investigated. Our conclusions are as follows.

(1) Under different L/D ratios and strain rates, the typical failure characteristics of limestone and slate were obtained to analyze the effect of L/D ratios and strain rates on rock mechanical parameters. As the L/D ratio increases, UCS and elastic

modulus show a non-linear decreasing trend, which is caused by the end effect of the rock sample. Variation of the strain rate changed the failure path, leading to the complexity of the rock failure type.

(2) A linear correlation between U^e and U, namely, the linear energy storage law, was found, along with a relationship between U^d and U^p. The linear energy characteristic has different correlations with strain rate and L/D as it is positively correlated with strain rate and negatively correlated with L/D. The W_{et} index was modified to the W_{et}^P index to allow assessment of rock burst proneness by considering energy dissipation in the post-peak stage of rock deformation. Combined with the failure characteristics of rock samples associated with the different conditions, the actual rock burst proneness can be classified into three grades: no risk (W_{et}^P below 2.5), low risk (W_{et}^P between 2.5 and 5.5), and high risk (W_{et}^P exceeding 5.5) to establish the criterion for rock burst.

(3) L/D ratio-dependent variation of the W_{et}^P index is similar to that of UCS. There is a platform stage in the relationship between W_{et}^P and strain rate, indicating that the rate-dependent growth in W_{et}^P has a critical value (0.1 to 1s^{-1}). The accuracy of rock burst proneness based on the W_{et}^P index was verified through comparison with existing criteria. The results suggest that W_{et}^P provides an effective description of rock burst proneness.

Data availability statement

Author contributions

XL: methodology and writing—original draft. YZ: software and formal analysis. HX: investigation and resources. LL: investigation and resources. HW: conceptualization, methodology, supervision, and writing—review and editing.

Acknowledgments

Conflict of interest

The authors XL was employed by Qinghai Traffic Construction Management Co., Ltd., and authors XL, HX, and LL were employed by Qinghai Xihu Expressway Management Co., Ltd.

The remaining authors declare that the research was conducted in the absence of any commercial or financial relationships that could be construed as a potential conflict of interest.

Publisher's note

All claims expressed in this article are solely those of the authors and do not necessarily represent those of their affiliated organizations, or those of the publisher, the editors, and the reviewers. Any product that may be evaluated in this article, or claim that may be made by its manufacturer, is not guaranteed or endorsed by the publisher.

References

Ai, C., Zhang, J., Li, Y. W., Zeng, J., Yang, X. L., and Wang, J. G. (2016). Estimation criteria for rock brittleness based on energy analysis during the rupturing process. *Rock Mech. Rock Eng.* 49 (12), 4681–4698. doi:10.1007/s00603-016-1078-x

Bukowska, M. (2005). Indicative methods for assessment of liability of rocks and rock mass to rock-bumps. *Res. Rep. Min. Environ.* 2, 95–107.

Cai, W., Dou, L. M., Si, G. Y., and Hu, Y. W. (2021). Fault-induced coal burst mechanism under mining-induced static and dynamic stresses. *Engineering-Prc.* 7 (5), 687–700. doi:10.1016/j.eng.2020.03.017

Cai, W. Q., Zhu, H. H., and Liang, W. H. (2022). Three-Dimensional tunnel face extrusion and reinforcement effects of underground excavations in deep rock masses. *Int. J. Rock Mech. Min. Sci.* 150, 104999. doi:10.1016/j.ijrmms.2021.104999

Cook, N. G. W. (1976). Seismicity associated with mining. *Eng. Geol.* 10, 99–122. doi:10.1016/0013-7952(76)90015-6

Dai, L. P., Pan, Y. S., Zhang, C. G., Wang, A. W., Canbulat, I., Shi, T. W., et al. (2022). New criterion of critical mining stress index for risk evaluation of roadway rockburst. *Rock Mech. Rock Eng.* 55 (8), 4783–4799. doi:10.1007/s00603-022-02888-7

Dai, S., Wang, X., Pan, Y., and Liu, L. (2019). Experimental study on the evaluation of coal burst tendency utilizing modulus index. *J. China Coal Soc.* 44 (6), 1726–1731.

Darbor, M., Faramarzi, L., and Sharifzadeh, M. (2019). Size-dependent compressive strength properties of hard rocks and rock-like cementitious brittle materials. *Geosystem Eng.* 22 (4), 179–192. doi:10.1080/12269328.2018.1431961

Diederichs, M. S. (2007). The 2003 Canadian geotechnical colloquium: Mechanistic interpretation and practical application of damage and spalling prediction criteria for deep tunnelling. *Can. Geotech. J.* 44 (9), 1082–1116. doi:10.1139/t07-033

Diederichs, M. S., Kaiser, P. K., and Eberhardt, E. (2004). Damage initiation and propagation in hard rock during tunnelling and the influence of near-face stress rotation. *Int. J. Rock Mech. Min. Sci.* 41 (5), 785–812. doi:10.1016/j.ijrmms.2004.02.003

Du, K., Tao, M., Li, X. B., and Zhou, J. (2016). Experimental study of slabbing and rockburst induced by true-triaxial unloading and local dynamic disturbance. *Rock Mech. Rock Eng.* 49 (9), 3437–3453. doi:10.1007/s00603-016-0990-4

Feng, G. L., Chen, B. R., Jiang, Q., Xiao, Y. X., Niu, W. J., and Li, P. X. (2021). Excavation-induced microseismicity and rockburst occurrence: Similarities and differences between deep parallel tunnels with alternating soft-hard strata. *J. Cent. South. Univ.* 28, 582–594. doi:10.1007/s11771-021-4623-z

Feng, G. L., Feng, X. T., Chen, B. R., Xiao, Y. X., and Yu, Y. (2015). A microseismic method for dynamic warning of rockburst development processes in tunnels. *Rock Mech. Rock Eng.* 48 (5), 2061–2076. doi:10.1007/s00603-014-0689-3

Gale, W. J. (2018). A review of energy associated with coal bursts. *Int. J. Min. Sci. Technol.* 28 (5), 755–761. doi:10.1016/j.ijmst.2018.08.004

Gong, F. Q., Luo, S., and Yan, J. Y. (2018c). Energy storage and dissipation evolution process and characteristics of marble in three tension-type failure tests. *Rock Mech. Rock Eng.* 51 (11), 3613–3624. doi:10.1007/s00603-018-1564-4

Gong, F. Q., Luo, Y., Li, X. B., Si, X. F., and Tao, M. (2018a). Experimental simulation investigation on rockburst induced by spalling failure in deep circular tunnels. *Tunn. Undergr. Space. Technol.* 81, 413–427. doi:10.1016/j.tust.2018.07.035

Gong, F. Q., Si, X. F., Li, X. B., and Wang, S. Y. (2018b). Experimental investigation of strain rockburst in circular caverns under deep three-dimensional high-stress conditions. *Rock Mech. Rock Eng.* 52, 1459–1474. doi:10.1007/s00603-018-1660-5

Gong, F. Q., Wang, Y. L., and Luo, S. (2020). Rockburst proneness criteria for rock materials: Review and new insights. *J. Cent. South Univ.* 27 (10), 2793–2821. doi:10.1007/s11771-020-4511-y

Gong, F. Q., Wang, Y. L., Wang, Z. G., Pan, J. F., and Luo, S. (2021). A new criterion of coal burst proneness based on the residual elastic energy index. *Int. J. Min. Sci. Tec.* 31, 553–563. doi:10.1016/j.ijmst.2021.04.001

Gong, F. Q., Yan, J. Y., Li, X., and Luo, S. (2019). A peak-strength strain energy storage index for rock burst proneness of rock materials. *Int. J. Rock Mech. Min. Sci.* 117, 76–89. doi:10.1016/j.ijrmms.2019.03.020

He, M. C., Sousa, L. R. E., Miranda, T., and Zhu, G. L. (2015). Rockburst laboratory tests database-application of data mining techniques. *Eng. Geol.* 185, 116–130. doi:10.1016/j.enggeo.2014.12.008

He, M. M., Wang, J., Yuan, Z. Y., Wang, H. T., Ma, X. D., and Luo, B. (2023). Evaluating the anisotropy of drilling mechanical characteristics of rock in the process of digital drilling. *Acta geophys.*, doi:10.1007/s00603-023-03242-1

Iman, R., Kivi, I. R., Ameri, M., and Molladavoodi, H. (2018). Shale brittleness evaluation based on energy balance analysis of stress-strain curves. *J. Pet. Sci. Eng.* 167, 1–19. doi:10.1016/j.petrol.2018.03.061

Kahraman, S. (2002). Correlation of TBM and drilling machine performances with rock brittleness. *Eng. Geol.* 65 (4), 269–283. doi:10.1016/s0013-7952(01)00137-5

Kaiser, P. K., and Cai, M. F. (2012). Design of rock support system under rockburst condition. *J. Rock Mech. Geotech. Eng.* 4, 215–227. doi:10.3724/sp.j.1235.2012.00215

Keneti, A., and Sainsbury, B. A. (2018). Review of published rockburst events and their contributing factors. *Eng. Geol.* 246, 361–373. doi:10.1016/j.enggeo.2018.10.005

Khosravi, A., and Simon, R. (2018). Verification of the CSDS model in estimating the postpeak behavior of hard rocks. *Int. J. Geomech.* 18 (3), 04017166. doi:10.1061/(asce)gm.1943-5622.0001090

Kidybiński, A. (1981). Bursting liability indices of coal. *Int. J. Rock Mech. Min. Sci.* 18, 295–304. doi:10.1016/0148-9062(81)91194-3

Kirane, K., Su, Y., and Bazõant, Z. P. (2015). Strain-rate-dependent micro plane model for high rate comminution of concrete under impact based on kinetic energy release theory. *Proc. R. Soc. A Math. Phys. Eng. Sci.* 471, 20150535. doi:10.1098/rspa.2015.0535

Konicek, P., and Waclawik, P. (2018). Stress changes and seismicity monitoring of hard coal longwall mining in high rockburst risk areas. *Tunn. Undergr. Space Technol.* 81, 237–251. doi:10.1016/j.tust.2018.07.019

Konsztowicz, K. J. (2010). Crack growth and acoustic emission in ceramics during thermal shock. *J. Am. Ceram. Soc.* 73 (3), 502–508. doi:10.1111/j.1151-2916.1990.tb06545.x

Li, S. J., Feng, X. T., Li, Z. H., Chen, B. R., Zhang, C. Q., and Zhou, H. (2012). *In situ* monitoring of rockburst nucleation and evolution in the deeply buried tunnels of Jinping II hydropower station. *Eng. Geol.* 137 (7), 85–96. doi:10.1016/j.enggeo.2012.03.010

Li, X. L., Chen, S. J., Liu, S. M., and Li, Z. H. (2021a). AE waveform characteristics of rock mass under uniaxial loading based on Hilbert-Huang transform. *J. Cent. South Univ.* 28 (6), 1843–1856. doi:10.1007/s11771-021-4734-6

Li, X. L., Chen, S. J., and Wang, S. (2021b). Study on *in situ* stress distribution law of the deep mine taking Linyi Mining area as an example. *Adv. Mater Sci. Eng.* 9 (4), 5594181.

Li, X. L., Zhang, X. Y., Shen, W. L., Zeng, Q., Chen, P., Qin, Q., et al. (2023). Research on the mechanism and control technology of coal wall sloughing in the ultra-large mining height working face. *Int. J. Env. Res. Pub He* 20 (2), 868. doi:10.3390/ijerph20010868

Li, Y., Huang, D., and Li, X. A. (2014). Strain rate dependency of coarse crystal marble under uniaxial compression: Strength, deformation and strain energy. *Rock Mech. Rock Eng.* 47 (4), 1153–1164. doi:10.1007/s00603-013-0472-x

Liu, H. Y., Zhang, B. Y., Li, X. L., Liu, C., Wang, C., Wang, F., et al. (2022). Research on roof damage mechanism and control technology of gob-side entry retaining under close distance gob. *Eng. Fail Anal.* 138 (5), 106331. doi:10.1016/j.engfailanal.2022.106331

Liu, S. M., Li, X. L., and Wang, D. K. (2020). Investigations on the mechanism of the microstructural evolution of different coal ranks under liquid nitrogen cold soaking. *Energy Sources, Part A Recovery, Util. Environ. Eff.* 17, 1. doi:10.1080/15567036.2020.1841856

Liu X L, X. L., Liu, Q., Liu, B., and Kang, Y. (2020). A modified bursting energy index for evaluating coal burst proneness and its application in ordos coalfield, China. *China. Energies* 13 (7), 1729. doi:10.3390/en13071729

Liu, X. Q., Wang, G., Song, L. B., Han, G. S., Chen, W. Z., and Chen, H. (2023). A new rockburst criterion of stress-strength ratio considering stress distribution of surrounding rock. *B Eng. Geol. Environ.* 82 (1), 29. doi:10.1007/s10064-022-03042-x

Lu, S., Xu, J. Y., Bai, E. L., and Luo, X. (2017). Effect of particles with different mechanical properties on the energy dissipation properties of concrete. *Constr. Build. Mat.* 144, 502–515. doi:10.1016/j.conbuildmat.2017.02.161

Lundborg, N. (1967). The strength-size relation of granite. *Int. J. Rock Mech. Min. Sci. Geomech. Abstr.* 4 (3), 269–272. doi:10.1016/0148-9062(67)90011-3

Luo, X., Xu, J. Y., Bai, E. L., and Li, W. (2014). Study on the effect of basalt fiber on the energy absorption characteristics of porous material. *Constr. Build. Mat.* 68 (6), 384–390. doi:10.1016/j.conbuildmat.2014.06.072

Malan, D. F., and Napier, J. A. L. (2018). Rockburst support in shallow-dipping tabular stopes at great depth. *Int. J. Rock Mech. Min. Sci.* 112, 302–312. doi:10.1016/j.ijrmms.2018.10.026

Małkowski, P., and Niedbalski, Z. (2020). A comprehensive geomechanical method for the assessment of rockburst hazards in underground mining. *Int. J. Min. Sci. Tech.* 30 (3), 345–355. doi:10.1016/j.ijmst.2020.04.009

Martin, C. D., and Maybee, W. G. (2000). The strength of hard-rock pillars. *Int. J. Rock Mech. Min. Sci.* 37 (8), 1239–1246. doi:10.1016/s1365-1609(00)00032-0

Masoumi, H., Saydam, S., and Hagan, P. C. (2016). Unified size-effect law for intact rock. *Int. J. Geomech.* 16 (2), 04015059. doi:10.1061/(asce)gm.1943-5622.0000543

Mazaira, A., and Konicek, P. (2015). Intense rockburst impacts in deep underground construction and their prevention. *Can. Geotech. J.* 52 (10), 1426–1439. doi:10.1139/cgj-2014-0359

Quiñones, J., Arzúa, J., Alejano, L., García-Bastante, F., Ivars, D. M., and Walton, G. (2017). Analysis of size effects on the geomechanical parameters of intact granite samples under unconfined conditions. *Acta. Geotech.* 12 (6), 1229–1242. doi:10.1007/s11440-017-0531-7

Rybacki, E., Meier, T., and Dresen, G. (2016). What controls the mechanical properties of shale rocks? – Part II: Brittleness. *J. Pet. Sci. Eng.* 144, 39–58. doi:10.1016/j.petrol.2016.02.022

Singh, S. P. (1989). Classification of mine workings according to their rockburst proneness. *Min. Sci. Technol.* 8, 253–262. doi:10.1016/s0167-9031(89)90404-0

Singh, S. P. (1988). Burst energy release index. *Rock Mech. Rock Eng.* 21 (2), 149–155. doi:10.1007/bf01043119

Sousa, L. R. E., Miranda, T., Sousa, R. L. E., and Tinoco, J. (2017). The use of data mining techniques in rockburst risk assessment. *Engineering-Prc* 3 (4), 552–558. doi:10.1016/j.eng.2017.04.002

Su, C. D. (2004). Testing study on the effect of crystal size and specimen length on the rockburst tendency. *China. J. Rock Mech. Eng.* 23 (22), 3750–3753.

Tang, L. Z., Pan, C. L., and Wang, W. X. (2002). Surplus energy index for analyzing rock burst proneness. *J. Cent. South Univ. Technol.* 33, 129–132.

Tarasov, B., and Potvin, Y. (2013). Universal criteria for rock brittleness estimation under triaxial compression. *Int. J. Rock Mech. Min.* 59, 57–69. doi:10.1016/j.ijrmms.2012.12.011

Tekalur, S. A., and Sen, O. (2011). Effect of specimen size in the Kolsky bar. *Procedia Eng.* 10, 2663–2671. doi:10.1016/j.proeng.2011.04.444

ISRM (2007). "The complete ISRM suggested methods for rock characterization, testing and monitoring: 1974–2006," in *Prepared by the commission on testing methods*. Editors R. Ulusay and J. A. Hudson (Ankara: ISRM).

Walton, G., Labrie, D., and Alejano, L. R. (2019). On the residual strength of rocks and rock masses. *Rock Mech. Rock Eng.* 52, 4821–4833. doi:10.1007/s00603-019-01879-5

Wang, H. T., He, M. M., Pang, F., Chen, Y., and Zhang, Z. (2021). Energy dissipation-based method for brittleness evolution and yield strength determination of rock. *J. Pet. Sci. Eng.* 200, 108376. doi:10.1016/j.petrol.2021.108376

Wang, H. T., He, M. M., Zhang, Z. Q., and Zhu, J. (2022a). Determination of the constant mi in the Hoek-Brown criterion of rock based on drilling parameters. *Int. J. Min. Sci. Techno.* 32 (4), 747–759. doi:10.1016/j.ijmst.2022.06.002

Wang, H. T., He, M. M., Zhu, J. W., Guo, S., and Chen, Y. (2022b). Experimental investigation of linear damping characteristics on granite and red sandstone under dynamic cyclic loading. *Eur. J. Environ. Civ. En.* 26 (11), 5259–5278. doi:10.1080/19648189.2021.1890230

Wang, H. T., and He, M. M. (2023a). Determining method of tensile strength of rock based on friction characteristics in the drilling process. *Rock Mech. Rock Eng*, doi:10.1007/s00603-023-03276-5

Wang, J., He, M. M., Yuan, Z. Y., Luo, B., and Ma, Y. D. (2023b). Ductile-brittle failure transition of rocks in process of drilling with high confining pressure: Model and experiment. *J. Pet. Sci. Eng.* 2023, 211505. doi:10.1016/j.geoen.2023.211505

Wang, J. A., and Park, H. D. (2001). Comprehensive prediction of rockburst based on analysis of strain energy in rocks. *Tunn. Undergr. Space Technol.* 16, 49–57. doi:10.1016/s0886-7798(01)00030-x

Wang, S. F., Li, X. B., Yao, J. R., Gong, F. Q., Li, X., Du, K., et al. (2019). Experimental investigation of rock breakage by a conical pick and its application to non-explosive mechanized mining in deep hard rock. *Int. J. Rock Mech. Min.* 122, 104063. doi:10.1016/j.ijrmms.2019.104063

Wasantha, P. L. P., Ranjith, P. G., Zhao, J., Shao, S. S., and Permata, G. (2015). Strain rate effect on the mechanical behaviour of sandstones with different grain sizes. *Rock Mech. Rock Eng.* 48 (5), 1883–1895. doi:10.1007/s00603-014-0688-4

Wei, M. D., Dai, F., Liu, Y., Li, A., and Yan, Z. L. (2021). Influences of loading method and notch type on rock fracture toughness measurements: From the perspectives of T-stress and fracture process zone. *Rock Mech. Rock Eng.* 54 (9), 4965–4986. doi:10.1007/s00603-021-02541-9

Wojtecki, L., Iwaszenko, S., Apel, D. B., and Cichy, T. (2021). An attempt to use machine learning algorithms to estimate the rockburst hazard in underground excavations of hard coal mine. *Energies* 14 (21), 6928. doi:10.3390/en14216928

Yang, B. B., He, M. M., Zhang, Z. Q., Zhu, J. W., and Chen, Y. S. (2022a). A new criterion of strain rockburst in consideration of the plastic zone of tunnel surrounding rock. *Rock Mech. Rock Eng.* 55 (3), 1777–1789. doi:10.1007/s00603-021-02725-3

Yang, F. J., Hui, Z., Xiao, H. B., Azhar, M. U., Yong, Z., and Chi, F. D. (2022b). Numerical simulation method for the process of rockburst. *Eng. Geol.* 306, 106760. doi:10.1016/j.enggeo.2022.106760

Yang, X., Ren, T., Tan, L., Remennikov, A., and He, X. (2018). Developing coal burst propensity index method for Australian coal mines. *Int. J. Min. Sci. Technol.* 28 (5), 783–790. doi:10.1016/j.ijmst.2018.08.008

Yumlu, M., and Ozbay, M. U. (1995). A study of the behaviour of brittle rocks under plane strain and triaxial loading conditions. *Int. J. Rock Mech. Min. Sci.* 32 (7), 725–733. doi:10.1016/0148-9062(95)00025-c

Zhang, X., Feng, G., Kang, L., and Yang, S. (2009). Method to determine burst tendency of coal rock by residual energy emission speed. *J. China Coal. Soc.* 34 (9), 1165–1168.

Zhou, X. M., Wang, S., Li, X. L., Meng, J., Li, Z., Zhang, L., et al. (2022). Research on theory and technology of floor heave control in semicoal rock roadway: Taking longhu coal mine in Qitaihe mining area as an Example. *Lithosphere-US* 11, 3810988. doi:10.2113/2022/3810988